2D Materials

PAPER

Epitaxial growth of monolayer $PdTe_2$ and patterned $PtTe_2$ by direct tellurization of Pd and Pt surfaces

To cite this article: Lina Liu *et al* 2021 *2D Mater.* **8** 045033

2D Materials

CrossMark

RECEIVED
13 April 2021

REVISED
15 June 2021

ACCEPTED FOR PUBLICATION
8 July 2021

PUBLISHED
4 October 2021

PAPER

Epitaxial growth of monolayer $PdTe_2$ and patterned $PtTe_2$ by direct tellurization of Pd and Pt surfaces

Lina Liu[1], **Dmitry Zemlyanov**[2,*] **and Yong P Chen**[1,2,3,4,5,*]

[1] Department of Physics and Astronomy, Purdue University, West Lafayette, IN 47907, United States of America
[2] Birck Nanotechnology Center, Purdue University, West Lafayette, IN 47907, United States of America
[3] Purdue Quantum Science and Engineering Institute and School of Electrical and Computer Engineering, Purdue University, West Lafayette, IN 47907, United States of America
[4] WPI-AIMR International Research Center on Materials Sciences, Tohoku University, Sendai 980-8577, Japan
[5] Institute of Physics and Astronomy and Villum Centers for Dirac Materials and for Hybrid Quantum Materials and Devices, Aarhus University, 8000 Aarhus-C, Denmark
[*] Authors to whom any correspondence should be addressed.

E-mail: dzemlian@puRdue.edu **and** yongchen@puRdue.edu

Keywords: 2D materials, TMDC, epitaxial growth, monolayer, plasmons, palladium ditelluride, platinum ditelluride

Supplementary material for this article is available online

Abstract

Two-dimensional (2D) palladium ditelluride ($PdTe_2$) and platinum ditelluride ($PtTe_2$) are two Dirac semimetals, which have fascinating quantum properties such as superconductivity, magnetism and topological order and show the promising applications in future nanoelectronics and optoelectronics. However, the synthesis of $PdTe_2$ and $PtTe_2$ monolayers (MLs) is hindered by a strong interlayer coupling and orbital hybridization. In this study, we demonstrate an efficient synthesis of $PdTe_2$ and $PtTe_2$ MLs Large-area and high quality MLs of $PdTe_2$ and patterned $PtTe_2$ were epitaxially grown on the Pd(111) and Pt(111) surfaces by direct telurization in ultra-high vacuum. This was confirmed by x-ray photoelectron spectroscopy, low energy electron diffraction and scanning tunnelling microscopy. $PdTe_2$ ML demonstrated high thermal stability showing no decomposition sign after annealing at 470 °C. A well-ordered (2×2) $PtTe_2$ structure with Kagome lattice was observed on Te/Pt(111) surface following annealing at 200 °C in UHV, where the (2×2) pattern was formed by Te atom vacancies. $PtTe_2$ multilayer film was prepared as well, and it demonstrated the excitation of the Dirac plasmons as measured by high-resolution electron energy loss spectroscopy. The direct tellurization offers the simple and reliable protocol for the preparation of the ML of $PdTe_2$ and patterned $PtTe_2$, and this opens new opportunities for quantum phenomena research and for practical optoelectronics applications.

1. Introduction

Two-dimensional (2D) noble transition metal dichalcogenides (NTMDs) are a subgroup of the 2D transition metal dichalcogenides (TMDCs), which exhibit the drastically different properties from most TMDCs [1]. NTMDs demonstrate a strong thickness-dependence of the band structure, high mobility, in-plane anisotropy and high air stability; these offer the exciting opportunities in nanoelectronics, optoelectronics and catalysis [2–9]. Type II Dirac fermions with superconductive properties were shown in $PdTe_2$, the coexistence of the superconductivity and the topological states at the 2D level creates a possibility to observe Majorana fermions [10–13]. The excitation of the 3D Dirac plasmons was observed in $PtTe_2$; and this makes this material a promising candidate for optoelectronic applications [14–16]. Both $PdTe_2$ and $PtTe_2$ show thickness-dependence of the band structure [17], which gives an opportunity to tune the electrical and optical properties of the materials. It is highly desirable to scale down the high-qualitive $PdTe_2$ and $PtTe_2$ to a monolayer (ML).

Unlike other TMDCs, $PdTe_2$ and $PtTe_2$ show a strong interlayer interaction due to their specific electronic configurations, where the *d* levels are nearly full occupation and the *p* levels are highly hybridized [17, 18]. This makes challenging to obtain ultrathin

2D layers using the 'top-down' methods such as a mechanical exfoliation. The traditional methods such as molecular beam epitaxy (MBE), chemical vapor deposition (CVD) and pulsed laser deposition were successfully used to grow different 2D materials demonstrating the promising 'bottom-up' approach [19–21]. Recently, the $PdTe_2$ and $PtTe_2$ flakes were synthesized by MBE, CVD and laser-assisted synthesis [22–25]. However, as prepared 2D flakes have the size in micrometre scale and present multilayer materials. Therefore, the synthesis of large-area, high-quality ML 2D films attracts significant attention. Large-area and high-quality ML of $PtSe_2$ was realized on the Pt(111) by selenium evaporation and sequential annealing in ultra-high vacuum (UHV) [26, 27]. A (3×3) superstructure was detected pointing to a strong interaction between $PtSe_2$ ML and the substrate [27]. Also, the intrinsically patterned 1T/1H $PtSe_2$ ML was observed during the epitaxial growth by controlling the concentration of defects [26].

Here we report in the first time the synthesis of the large-area $PdTe_2$ and $PtTe_2$ ML films by direct tellurization of the Pd(111) and Pt(111) surfaces. Using a one-step approach, we obtained high-quality ML films as confirmed by scanning tunnelling microscopy (STM), x-ray photoelectron spectroscopy (XPS) and low-energy electron diffraction (LEED). In the case of $PtTe_2$, a (2×2) structure with Kagome lattice was observed demonstrating the well-ordered vacancies of Te atoms in the topmost layer of $PtTe_2$. Multilayer of $PtTe_2$ was also obtained by this method and the excitation of Dirac plasmons was detected by high-resolution electron energy loss spectroscopy (HREELS). The reliable synthesis of the $PdTe_2$ and patterned $PtTe_2$ MLs open new application opportunities in electronics and optoelectronics.

2. Method

All experiments were performed using an Omicron Surface Analysis Cluster, which was described elsewhere [28–30]. The setup consists of an UHV preparation chamber and UHV μ-metal analysis chamber with base pressures of 1×10^{-9} mbar and 5×10^{-11} mbar, respectively. Pd(111) and Pt(111) single crystals with 9 mm of diameter, 1 mm of thickness and with orientation accuracy <0.5° (MaTecK GmbH) were cleaned by repeated cycles of Ar^+ sputtering and annealing in UHV at 780 °C. The surface cleanliness was monitored by XPS, LEED, and STM. For each deposition experiment, the single crystals were freshly cleaned. Tellurium (99.999%, Sigma-Aldrich) was thermally evaporated using a home-built evaporator in the preparation chamber. The tellurium temperature in the evaporation regime was in the range of 290 °C–300 °C and the evaporation rate was controlled by the heater power. The substrate was kept at room temperature (RT) during Te deposition. The amount of deposited tellurium was verified by XPS. The details of thickness of deposited Te and deposition time are shown in figure S1 (available online at stacks.iop.org/2DM/8/045033/mmedia). The sample temperature was measured by a K-type thermocouple attached to the manipulator part with which a sample holder was in a good thermal contact. To complete the telluride synthesis, a single crystal was annealed at the specified temperature for 10 min in UHV.

STM images (Omicron ambient temperature UHV STM) were collected at RT using electrochemically etched W and Pt-Ir tips at constant current (topographic) mode. In all experiments reported here, the tip was electrically grounded, meaning that at positive bias the electrons flowed from the tip to the sample. The STM images were analyzed using WSxM software [31].

XPS was acquired using a non-monochromatic Mg Kα x-ray radiation ($h\nu = 1253.6$ eV) at 150 W. High resolution spectra were recorded at constant pass energy of 20 eV using the electron energy analyzer-Omicron EAC 125 and the analyzer controller-Omicron EAC 2000. The resolution of the instrument/sample system, which was measured as the full width at half maximum of Pt $4f_{7/2}$ peaks of the clean Pt(111) crystal, was approximately 1.2 eV. Photoelectrons were collected at a 45° angle with respect to the surface normal. The parameters used for the calculation of practical electron attenuation lengths (EALs) using NIST database tool [32] are shown in table S1 in the supporting information (SI).

LEED measurements were conducted in the analyst chamber straight after sample preparation with a four-grid optics (Omicron LEED).

3. Results and discussion

$PdTe_2$ and $PtTe_2$ MLs were grown by deposition of Te on the Pd(111) and Pt(111) surfaces followed by annealing under UHV conditions. The schematic cartoon of the process is shown in figure 1. HREELS spectra confirm the formation of $PdTe_2$ and $PtTe_2$ (figure S2). On $PdTe_2$, HREELS losses were observed at 15 meV and 25 meV in agreement with the optical modes reported for $PdTe_2$ bulk crystal [33]. The mode of $PtTe_2$ shows a single vibration at 21 meV, which also follows the phonon dispersion features of $PtTe_2$ [34].

The different annealing temperature is required for $PdTe_2$ and $PtTe_2$ to get a flat and high-quality surface. Thus, a large-area $PdTe_2$ ML film was obtained after annealing at 470 °C (figure 2(b)), whereas the reasonably flat surface of $PtTe_2$ was obtained following annealing at 200 °C (figure 2(f)). For $PdTe_2$, the surface annealed at low temperatures was covered

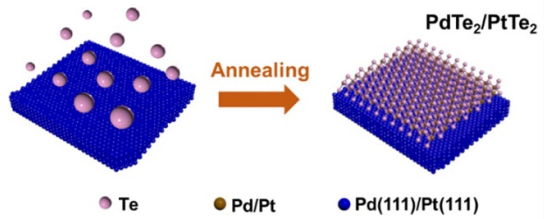

Figure 1. Schematic process of epitaxial growth of monolayer $PdTe_2$ and patterned $PtTe_2$ on single crystal Pd (111) or Pt (111) by tellurization.

by small irregularly shaped islands although STM showed the atomic arrangement corresponding to $PdTe_2$ (figure S3(a)). Below we focus on the conditions giving the best growth results, which corresponds to the annealing temperature of 470 °C. LEED of $PdTe_2$ ML obtained following 470 °C annealing shows a hexagonal diffraction pattern confirming a high crystallinity the (1 × 1) $PdTe_2$ structure over a large area (insets of figures 2(b) and S4(a)). Moreover, LEED analysis performed at the multiple spots is fully consistent with this conclusion (figure S4). LEED indicates that the $PdTe_2$ film has the same crystalline orientation across the entire surface. This allows to conclude that a large area of $PdTe_2$ ML of several mm size was prepared. The high-resolution STM image in figure 2(c) demonstrates the atomic structures of $PdTe_2$ with a hexagonal arrangement of the Te atoms in the topmost layer. An interatomic distance of 4.7 Å (figure 2(d)) corresponds to $\sqrt{3}\times\sqrt{3}$ arrangement for Pd(111) ($\sqrt{3}\times 2.75 = 4.76$ Å). The $PdTe_2$ lattice is rotated by 30° with respect to the underlying Pd(111) substrate, aligning one of the unit vectors of $PdTe_2$ with the $[\bar{1}12]$ direction of the Pd(111) substrate (figure S5). The $\sqrt{3}\times\sqrt{3}$ arrangement could be thermodynamically driven to match the fcc or hcp sites of underlying Pd(111) substrate.

In the case of $PtTe_2$, a ML film was obtained following annealing at the temperature of 200 °C. The prepared surface was flat, only a few nanoparticles and the decoration of a monoatomic step was observed by STM (figure 2(f)). Unlike the (1 × 1) structure observed on $PdTe_2$/Pd(111), LEED displays a hexagonal diffraction (2 × 2) pattern on the $PtTe_2$ surface (inset of figure 2(f)). The STM image in figure 2(g) shows atomic vacancies, which look like dark spots, forming the hexagonal structure with a periodicity of 8.2 Å (the line profile in figure 2(h)), which is approximately two times by the expected lattice parameter for $PtTe_2$ [35, 36]. This (2 × 2) $PtTe_2$ represents the Kagome lattice as shown by two green triangles in figure 2(g). These atomic vacancies are the ordered defects due to missing Te atoms in the topmost layer of $PtTe_2$. The size of the (2 × 2) $PtTe_2$ structure approximately matches three times of Pt(111) lattice (2 × 4.1 Å ≈ 3 × 2.77 Å = 8.31 Å). The (2 × 2) $PtTe_2$ is aligned with the underlying Pt(111) having one of the unit cell vectors parallel with the $[\bar{1}10]$ direction of Pt(111). This was concluded based on the LEED observation (figure S6). Therefore, we can suppose that the generated Te vacancies rearrange into the (2 × 2) pattern, which is driven thermodynamically to match the fcc or hcp sites of the underlying Pt(111) lattice. According to STM, in the (2 × 2) structure, one of four Te atoms of the topmost layer is missing, therefore, the formal stoichiometry should be $PtTe_{1.75}$. The (2 × 2) structure demonstrates high thermal stability. LEED does not change and remains the (2 × 2) patterns following annealing at 500 °C in UHV (figure S7(a)). The atomic resolution STM image shows that the (2 × 2) $PtTe_2$ is still mainly intact although a few defects are generated (figures S7(b)–(d)). We would like to underline that the (2 × 2) structure is unique and only observed for $PtTe_2$ and not for $PdTe_2$. To the best of our knowledge, the (2 × 2) structure was not reported before.

Chemical sensitivity of XPS was used to confirm the formation of $PdTe_2$ and $PtTe_2$. Following Te deposition at RT on Pd(111), the centroids of the Pd $3d_{5/2}$ and Pd $3d_{3/2}$ peaks were at 335.6 eV and 340.9 eV, respectively, which shift towards higher binding energies (BEs) by 0.5 eV with respect to those of clean Pd(111) (figures 3(a) and S8(a)). This indicates the formation of the Pd-Te chemical bond right after Te deposition, and it points to a low activation barrier for the reaction between Pd and Te. The surface cleanliness is an important factor to promote the reaction. Impinging tellurium atoms can easily interact with the surface of the noble metal creating the chemical bond. The formation of $PdTe_x$ particles with the size of approximately 2 nm was detected following deposition as shown in figure S9. The annealing at 470 °C in UHV leads to the decreasing of the Te amount and, the centroid of the Pd $3d_{5/2}$ peak shifts back to 335.1 eV. This is because the contribution of Pd(111) bulk dominates in the XPS signal and the contribution of $PdTe_2$ ML is difficult to be separated. On the other hand, the annealing results in the shift of the Te 3d peaks towards lower BEs by 0.2 eV, which points to the further transfer of the electron density from Pd to Te confirming the formation of $PdTe_2$ (figure 3(b)). In the case of Te/Pt(111), the annealing at 200 °C does not lead to the shift of the Pt 4f and Te 3d peaks (figures 3(c), (d) and S8(b)). For both $PdTe_2$ and $PtTe_2$, the Te $3d_{5/2}$ peak at 573.3 eV (figures 3(a) and (c)) is higher by approximately 0.5 eV comparing to the bulk materials [23, 24]. This could be attributed to charge transfer between the epitaxial grown MLs and the substrates due to differences in the work functions [37, 38].

The thickness of the as-grown films was calculated using XPS data analysed with a XPS Thickness Solver tool from Nanohub [39]. XPS thickness model is discussed in detail elsewhere [30, 40]. This

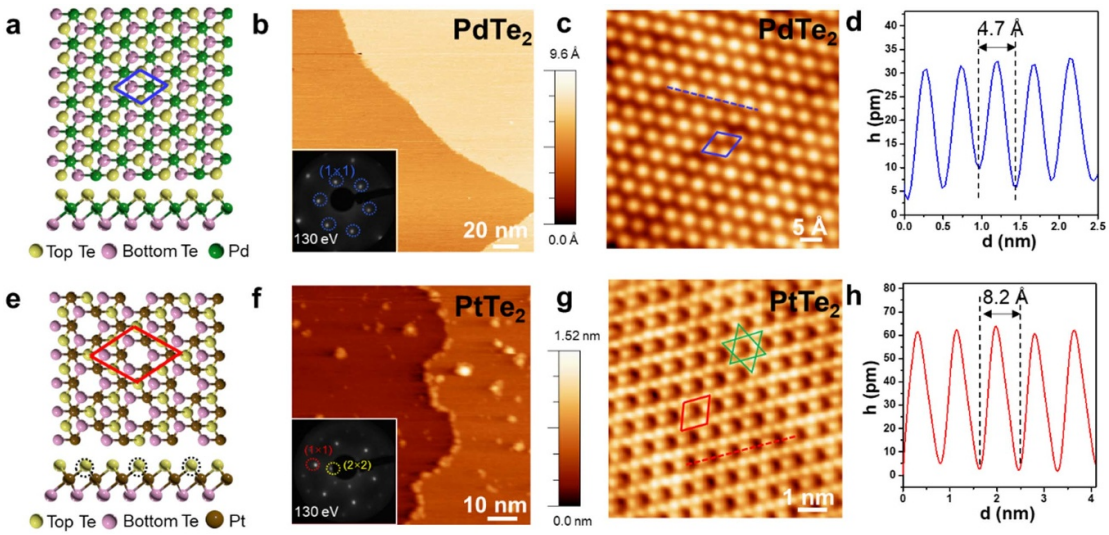

Figure 2. Epitaxial growth of monolayer $PdTe_2$ and patterned $PtTe_2$: (a), (e) cartoon presentation (top and side views) of $PdTe_2$ and patterned $PtTe_2$, respectively. The missing Te atoms in the patterned $PtTe_2$ are marked with the black dashed circles in the side view of (e). (b), (f) Typical STM images of the $PdTe_2$ and patterned $PtTe_2$ films, respectively. The scanning parameters for (b) were $V_b = 0.8$ V, $I_t = 0.7$ nA and for (f) were $V_b = -0.5$ V, $I_t = 1.6$ nA. Insets: LEED patterns of $PdTe_2$ and patterned $PtTe_2$, respectively; the blue dashed circles indicate the reflexes for the (1×1) $PdTe_2$ corresponding to the unit cell (blue diamond) in (c); the red dashed circles in (f) are for the unit cell of $PtTe_2$ drawn as a red diamond in (g) and the yellow dashed circles are for the (2×2) arrangements of the holes in (g). (c), (g) Atomic resolution STM images of $PdTe_2$ and $PtTe_2$, respectively, the scanning parameters were similar to (b), (f). (d), (h) Line profiles of $PdTe_2$ and patterned $PtTe_2$ corresponding to the blue and red dashed lines in (c) and (g), respectively. The green triangles in (g) represent the Kagome lattice of the patterned $PtTe_2$.

approach was proposed by Fadley [41]. The equation for the overlayer thickness, t, can be written as

$$\frac{N_l(\theta)}{N_s(\theta)} = \frac{\rho_l \times \frac{d\sigma_l}{d\Omega} \times \Lambda_l(E_l) \times \cos\theta}{\rho_s \times \frac{d\sigma_s}{d\Omega} \times \Lambda_s(E_s) \times \cos\theta} \times \frac{\left(1 - \exp\left(\frac{-t}{\Lambda_l(E_l)\times\cos\theta}\right)\right)}{\left(\exp\left(\frac{-t}{\Lambda_l(E_s)\times\cos\theta}\right)\right)} \quad (1)$$

where $N_l(\theta)$ and $N_s(\theta)$ are the photoemission peak areas of the overlayer (l is for Te 3d in our case) and the substrate (s is for Pd 3d or Pt 4f in our case) at the given photoemission angle, θ, measured in respect to the surface normal. ρ_l and ρ_s are the numbers of atoms per unit volume (density) for the overlayer and substrate. $(d\sigma_l/d\Omega)$ and $(d\sigma_s/d\Omega)$ are differential cross-sections for the overlayer and substrate photoemission peaks. This numbers can be calculated using the Scofield cross sections [42] and the Reilman asymmetry parameter [43]. Instead of the inelastic mean free paths in the original [41], we use the EAL: $\Lambda_l(E_l)$ for the photoelectrons originated in the overlayer and attenuated in the overlayer, $\Lambda_s(E_s)$ for the photoelectrons originated in the substrate and attenuated in the substrate, and $\Lambda_l(E_s)$ for the photoelectrons originated in the substrate and attenuated in the overlayer. All EALs were calculated using NIST SRD-82 [32]. Equation (1) was solved numerically using the Nanohub tool [39]. In the [40], the Nanohub tool was validated for the thickness calculation of TMDC materials such as MoS_2, and the results were crosschecked by transition electron microscopy.

The intensity ratio between the photoemission peaks obtained from the MoS_2 films such as Mo 3d, S 2s and S 2p and the Al 2p peaks from the substrate was used as the primary input parameter for the thickness calculation in the [40]. In our case, the photoemission peaks of Pt and Pd from NTMDs cannot be separated from substrates. Therefore, we have simplified the system. For the calculation, we have considered the $PdTe_2$ ($PtTe_2$) overlayer as Te overlayer as shown in figure S10. The as-calculated thicknesses of the Te overlayers were 2.37 Å and 2.48 Å for $PdTe_2$ and $PtTe_2$, respectively. To verify if these numbers correspond to ML, the ML $PtSe_2$ on Pt(111) was used as a reference because of the similar structural construction with our system. By following the recipe from [26, 27], ML $PtSe_2$ was grown on Pt(111) confirmed by STM, LEED and XPS (figure S11). Using the same calculation method, the thickness of Se overlayer was 2.26 Å, which corresponds to the $PtSe_2$ ML on Pt(111) and can be used as a reference value for our system. The ratio between 2.37 Å and 2.26 Å is 1.05, corresponding to 1.05 ML for $PdTe_2$ on Pd(111). The $PtTe_2$ on Pt(111) estimated in the same way is 1.10 ML. Therefore, the conclusion is that in both cases the MLs of $PdTe_2$ and $PtTe_2$ were successfully grown. On the other hand, no bilayer or multilayer areas were detected by STM, also confirming the ML natures. The step height was approximately 2.2 Å (figure S12), matching a monoatomic step of Pd(111) or Pt(111) and

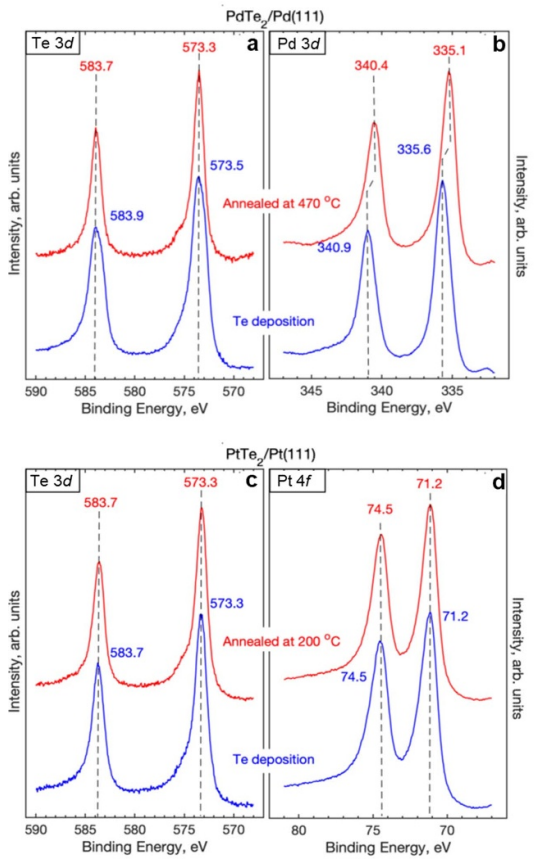

Figure 3. XPS spectra of $PdTe_2$ (the top row) and patterned $PtTe_2$ (the bottom row). (a), (b) The Te 3d and Pd 3d peaks obtained after deposition of Te (blue) and following annealing at 470 °C (red), respectively. (c), (d) Te 3d and Pt 4f peaks obtained after deposition of Te (blue) and following annealing at 200 °C (red), respectively.

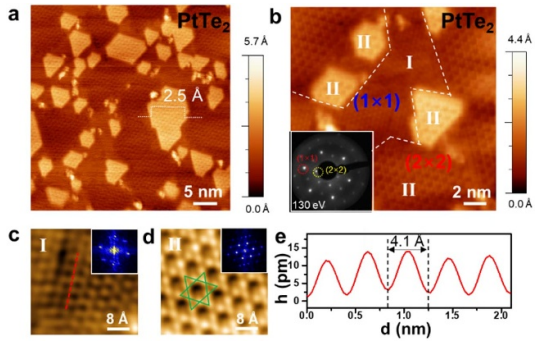

Figure 4. (a) A typical STM image of the $PtTe_2$ monolayer obtained at annealing temperature of 100 °C. (b) A zoom-in STM image of (a) and the inset shows the observed LEED pattern. The white dashed lines are 'guide for the eye' of the boundary between structure I and structure II on the terrace. Structure II exists both inside and outside of the islands. The red and yellow circles indicate in the LEED pattern the (1 × 1) and (2 × 2) reflexes, respectively. (c), (d) Atomic resolution STM images of the (1 × 1) and (2 × 2) $PtTe_2$ structures, respectively. The green triangles in (d) show the Kagome lattice. The insets of (c) and (d) demonstrate fast Fourier transform (FFT) of each image. (e) A line profile corresponding to the red dashed line in (c). The tunnelling conditions were $V_b = -1.1$ V, $I_t = 0.9$ nA.

pointing to that $PdTe_2$ or $PtTe_2$ was grown epitaxially as a single layer.

The annealing temperature plays an important role in the $PdTe_2$ and $PtTe_2$ synthesis. Following the annealing at the temperature of 100 °C, the Te/Pd(111) and Te/Pt(111) surfaces are not flat and are covered with islands (figures 4(a) and S3(a)). The formation of the islands with an irregular shape indicates a non-thermodynamic equilibrium growth. Atomic structures of $PdTe_2$ can be resolved on top of the islands and on the terraces following the annealing even at of 100 °C (inset of figure S3(a) in the SI), further confirming the low activation barrier of the reaction between Pd and Te. Likely, the $PdTe_2$ ML film covers the surface as a 'carpet'.

The Pt–Te interaction is more complex. Following the annealing at 100 °C, two atomic structures labelled with 'I' and 'II' were detected by STM (figure 4(a) and (b)). Structure I exhibits hexagonal atomic arrangements with the periodicity of 4.1 Å (figures 4(c) and (e)), which corresponds to the normal $PtTe_2$ lattice [35, 36], and we refer to this structure as a (1 × 1) $PtTe_2$. Typically, this phase is observed outside of the islands on the terraces. Structure II is the discussed above (2 × 2) $PtTe_2$ Kagome lattice (figure 4(d)). LEED patterns show bright (1 × 1) and weak (2 × 2) diffraction spots, confirming the coexistence of the two structures across a large area (inset of figure 4(b)). The (1 × 1) phase of $PtTe_2$ has higher surface density of Te comparing to the (2 × 2) structure. However, the latter is more thermodynamically stable: the (2 × 2) phase dominates completely following the annealing at 200 °C. Moreover, the 500 °C annealing in UHV did not affect much the (2 × 2) $PtTe_2$ phase, STM detects only a few atomic defects appeared on the surface (figure S7).

The $PtTe_2$ multilayer film was grown by the substantial increasing of the deposited amount of Te (figure 5(a)). The thickness calculated based on the XPS results was estimated to be approximately four $PtTe_2$ layers. The height of the step of multilayer $PtTe_2$ is 5.0 Å, (inset of figure 5(a)) corresponding to c lattice constant of $PtTe_2$ [14]. The $PtTe_2$ multilayer is characterized by the Pt $4f_{7/2}$ and $4f_{5/2}$ peaks at 71.6 eV and 74.9 eV, respectively (figure S13). These positions are shifted towards the higher BEs by 0.4 eV comparing to the ML case. Meanwhile, the Te $3d_{5/2}$ and $3d_{3/2}$ peaks are at 572.8 eV and 583.2 eV, which are shifted towards lower BEs by 0.5 eV comparing to the ML case. The BEs of the Te 3d peaks are consistent with the values reported in the literature for $PtTe_2$ [23]. This also confirms our hypothesis about the charge transfer between the Pt(111) substrate and the $PtTe_2$ ML. The atomic structure of the $PtTe_2$ multilayer has the periodicity of 4.1 Å (figure 5(b)) corresponding to the lattice constant of $PtTe_2$ [36]. LEED shows the typical (1 × 1) diffraction patterns (inset of figure 5(b)) indicating the high crystallinity across

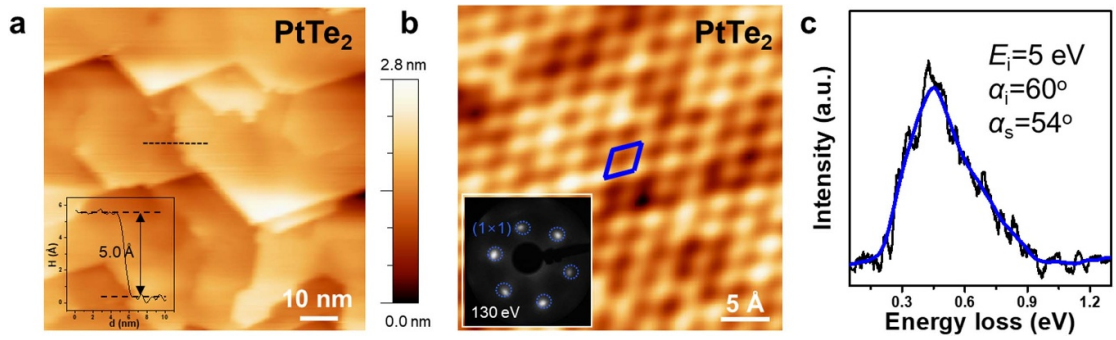

Figure 5. Multilayer $PtTe_2$. (a) A STM topographic image of multilayer $PtTe_2$. The tunnelling conditions are $V_b = -1.1$ V, $I_t = 0.8$ nA. Inset: a height profile along the black dashed line in (a). (b) Atomic resolution STM image of the multilayer $PtTe_2$. The blue rhombus indicates a unit cell. The tunnelling conditions are $V_b = 0.9$ V, $I_t = 0.7$ nA. Inset: LEED patterns of the multilayer $PtTe_2$. The blue dashed circles indicate the (1×1) reflexes. (c) HREELS spectrum of the multilayer $PtTe_2$ (after background subtraction). The blue line is 'guide for the eye'. The kinetic energy of the electron beam (E_i) is 5 eV. The incident angle (α_i) and scattering angle (α_s) for the HREELS measurement are 60° and 54°, respectively.

a large surface area. Notably, the excitation spectrum of multilayer $PtTe_2$ was obtained by HREELS (figure 5(c)) and it shows potential excitation of Dirac plasmons (figure S14). This confirms the high quality of the $PtTe_2$ multilayer and demonstrates its potential in the optoelectronics application. The successful growth of ML and multilayer of $PtTe_2$ provides a significant platform for investigating the unique layer-dependent properties of this material.

4. Conclusions

We demonstrate the epitaxial growth of the ML of $PdTe_2$ and patterned $PtTe_2$ by direct tellurium deposition on the Pd(111) and Pt(111) surfaces; the synthesis was established by STM, XPS and LEED. The large-area high quality $PdTe_2$ and patterned $PtTe_2$ ML films were prepared following the annealing in UHV at the temperatures of 470 °C and 200 °C, respectively. The $PdTe_2$ exhibits the hexagonal structure with the atomic spacing of 4.7 Å. This ML was fully formed following the annealing at 470 °C. Contrary to the 'single' (1×1) $PdTe_2$ structure, $PtTe_2$ demonstrates two phases. The (2×2) $PtTe_2$ structure was more thermodynamically stable than the (1×1) $PtTe_2$ phase, the latter of which was observed after the annealing at 100 °C. The (2×2) pattern was formed by well-ordered Te atomic vacancies arranged as the Kagome lattice and it completely dominated following the 200 °C annealing. This structure did not show the signs of degradation following the annealing at 500 °C. XPS confirms the ML nature of the epitaxial-grown films. High quality $PtTe_2$ multilayer film was obtained by the increasing of the amount of the deposited Te. HREELS measured the excitation of plasmons on the multilayer film of $PtTe_2$. This simple and robust synthesis of the large area 2D materials opens new opportunities for novel quantum phenomena research and for the potential applications in optoelectronics.

Data availability statement

All data that support the findings of this study are included within the article (and any supplementary files).

Acknowledgments

We acknowledge the partial financial support by the U.S. Department of Energy (Office of Basic Energy Sciences) under Award No. DE-SC0019215 and Multidisciplinary University Research Initiatives (MURI) Program under Award No. FA9550-20-1-0322. We thank Prof. Ronald G Reifenberger for fruitful discussions. We express our gratitude to the Center for Nanoscale Materials and in particularly to Dr Nathan P Guisinger for the help with the STM tip preparation (the Center for Nanoscale Materials, an Office of Science user facility, is supported by the U.S. Department of Energy, Office of Science, Office of Basic Energy Sciences, under Contract No. DE-AC02-06CH11357).

ORCID iD

Dmitry Zemlyanov https://orcid.org/0000-0002-1221-9195

References

[1] Pi L, Li L, Liu K L, Zhang Q F, Li H Q and Zhai T V 2019 Recent progress on 2D noble-transition-metal dichalcogenides *Adv. Funct. Mater.* **29** 1904932
[2] Chia X, Adriano A, Lazar P, Sofer Z, Luxa J and Pumera M 2016 Layered platinum dichalcogenides (PtS_2, $PtSe_2$, and $PtTe_2$) electrocatalysis: monotonic dependence on the chalcogen size *Adv. Funct. Mater.* **26** 4306–18
[3] Ciarrocchi A, Avsar A, Ovchinnikov D and Kis A 2018 Thickness-modulated metal-to-semiconductor transformation in a transition metal dichalcogenide *Nat. Commun.* **9** 919

[4] Oyedele A D *et al* 2019 Defect-mediated phase transformation in anisotropic two-dimensional $PdSe_2$ crystals for seamless electrical contacts *J. Am. Chem. Soc.* **141** 8928–36

[5] Jiang S *et al* 2019 Anisotropic growth and scanning tunneling microscopy identification of ultrathin even-layered $PdSe_2$ ribbons *Small* **15** 1902789

[6] Avsar A, Ciarrocchi A, Pizzochero M, Unuchek D, Yazyev O V and Kis A 2019 Defect induced, layer-modulated magnetism in ultrathin metallic $PtSe_2$ *Nat. Nanotechnol.* **14** 674–8

[7] Yu X *et al* 2018 Atomically thin noble metal dichalcogenide: a broadband mid-infrared semiconductor *Nat. Commun.* **9** 1545

[8] Hu D *et al* 2019 Unveiling the layer-dependent catalytic activity of $PtSe_2$ atomic crystals for the hydrogen evolution reaction *Angew. Chem., Int. Ed.* **58** 6977–81

[9] Okogbue E, Ko T J, Han S S, Shawkat M S, Wang M, Chung H S, Oh K H and Jung Y 2020 Wafer-scale 2D $PtTe_2$ layers for high-efficiency mechanically flexible electro-thermal smart window applications *Nanoscale* **12** 10647–55

[10] Xue H, Yang H, Wu Y, Yao G, Guan D, Wang S, Zheng H, Liu C, Li Y and Jia J 2019 Molecular beam epitaxy of superconducting $PdTe_2$ films on topological insulator Bi_2Te_3 *Sci. China: Phys. Mech. Astron.* **62** 076801

[11] Clark O J *et al* 2018 Fermiology and superconductivity of topological surface states in $PdTe_2$ *Phys. Rev. Lett.* **120** 156401

[12] Wang M X *et al* 2012 The coexistence of superconductivity and topological order in the Bi_2Se_3 thin films *Science* **336** 52–55

[13] Timmons E I *et al* 2020 Electron irradiation effects on superconductivity in $PdTe_2$: an application of a generalized Anderson theorem *Phys. Rev. Res.* **2** 023140

[14] Politano A, Chiarello G, Ghosh B, Sadhukhan K, Kuo C N, Lue C S, Pellegrini V and Agarwal A 2018 3D Dirac plasmons in the type-II Dirac semimetal $PtTe_2$ *Phys. Rev. Lett.* **121** 086804

[15] Yan M *et al* 2017 Lorentz-violating type-II Dirac fermions in transition metal dichalcogenide $PtTe_2$ *Nat. Commun.* **8** 257

[16] Zeng L, Wu D, Jie J, Ren X, Hu X, Lau S P, Chai Y and Tsang Y H 2020 Van der Waals epitaxial growth of mosaic-like 2D platinum ditelluride layers for room-temperature mid-infrared photodetection up to 10.6 microm *Adv. Mater.* **32** 2004412

[17] Villaos R A B, Crisostomo C P, Huang Z Q, Huang S M, Padama A A B, Albao M A, Lin H and Chuang F C 2019 Thickness dependent electronic properties of Pt dichalcogenides *NPJ 2D Mater. Appl.* **3** 2

[18] Yang H, Kim S W, Chhowalla M and Lee Y H 2017 Structural and quantum-state phase transitions in van der Waals layered materials *Nat. Phys.* **13** 931–7

[19] Liu C W *et al* 2020 Substrate-induced strain in 2D layered GaSe materials grown by molecular beam epitaxy *Sci. Rep.* **10** 12972

[20] Yi K, Liu D, Chen X, Yang J, Wei D, Liu Y and Wei D 2021 Plasma-enhanced chemical vapor deposition of two-dimensional materials for applications *Acc. Chem. Res.* **54** 1011–22

[21] Yao J D, Zheng Z Q and Yang G W 2019 Production of large-area 2D materials for high-performance photodetectors by pulsed-laser deposition *Prog. Mater. Sci.* **106** 100573

[22] Ma H *et al* 2018 Thickness-tunable synthesis of ultrathin type-II Dirac semimetal $PtTe_2$ single crystals and their thickness-dependent electronic properties *Nano Lett.* **18** 3523–9

[23] Fu L, Hu D, Mendes R G, Rummeli M H, Dai Q, Wu B, Fu L and Liu Y 2018 Highly organized epitaxy of Dirac semimetallic $PtTe_2$ crystals with extrahigh conductivity and visible surface plasmons at edges *ACS Nano* **12** 9405–11

[24] Li E *et al* 2018 High quality $PdTe_2$ thin films grown by molecular beam epitaxy *Chin. Phys.* B **27** 086804

[25] Nguyen D A, Park D Y, Lee J, Duong N T, Park C, Nguyen D H, Le T S, Suh D, Yang H and Jeong M S 2021 Patterning of type-II Dirac semimetal $PtTe_2$ for optimized interface of tellurene optoelectronic device *Nano Energy* **86** 106049

[26] Lin X *et al* 2017 Intrinsically patterned two-dimensional materials for selective adsorption of molecules and nanoclusters *Nat. Mater.* **16** 717–21

[27] Wang Y *et al* 2015 Monolayer $PtSe_2$, a new semiconducting transition-metal-dichalcogenide, epitaxially grown by direct selenization of Pt *Nano Lett.* **15** 4013–8

[28] Paul R, Reifenberger R G, Fisher T S and Zemlyanov D Y 2015 Atomic layer deposition of FeO on Pt(111) by ferrocene adsorption and oxidation *Chem. Mater.* **27** 5915–24

[29] Gharachorlou A, Detwiler M D, Mayr L, Gu X K, Greeley J, Reifenberger R G, Delgass W N, Ribeiro F H and Zemlyanov D Y 2015 Surface chemistry of trimethylaluminum on Pd(111) and Pt(111) *J. Phys. Chem.* C **119** 19059–72

[30] Gharachorlou A, Detwiler M D, Nartova A V, Lei Y, Lu J, Elam J W, Delgass W N, Ribeiro F H and Zemlyanov D Y 2014 Palladium nanoparticle formation on TiO_2(110) by thermal decomposition of palladium(II) hexafluoroacetylacetonate *ACS Appl. Mater. Interfaces* **6** 14702–11

[31] Horcas I, Fernandez R, Gomez-Rodriguez J M, Colchero J, Gomez-Herrero J and Baro A M 2007 WSXM: a software for scanning probe microscopy and a tool for nanotechnology *Rev. Sci. Instrum.* **78** 013705

[32] Powell C J and Jablonski A 2011 *NIST Electron Effective-Attenuation-Length Database, Version1.3, SRD 82* (Gaithersburg, MD: National Institute of Standards and Technology)

[33] D'Olimpio G, Guo C, Kuo C-N, Edla R, Lue C S, Ottaviano L, Torelli P, Wang L, Boukhvalov D W and Politano A 2020 $PdTe_2$ transition-metal dichalcogenide: chemical reactivity, thermal stability, and device implementation *Adv. Funct. Mater.* **30** 1906556

[34] Kim K, Kim S, Kim J S, Kim H, Park J-H and Min B I 2018 Importance of the van Hove singularity in superconducting $PdTe_2$ *Phys. Rev.* B **97** 165102

[35] Kliche G 1985 Far-infrared and x-ray investigations of the mixed platinum dichalcogenides $PtS_{2-x}Se_x$, $PtSe_{2-x}Te_x$, and $PtS_{2-x}Te_x$ *J. Solid State Chem.* **56** 26–31

[36] Hao S *et al* 2018 Low-temperature eutectic synthesis of $PtTe_2$ with weak antilocalization and controlled layer thinning *Adv. Funct. Mater.* **28** 1803746

[37] Xiong W, Huang K and Yuan S 2019 The mechanical, electronic and optical properties of two-dimensional transition metal chalcogenides MX_2 and M_2X_3 (M = Ni, Pd; X = S, Se, Te) with hexagonal and orthorhombic structures *J. Mater. Chem.* C **7** 13518–25

[38] Michaelson H B 1977 The work function of the elements and its periodicity *J. Appl. Phys.* **48** 4729–33

[39] Smith K C, Saenz D A, Zemlyanov D and Voevodin A 2012 XPS thickness solver

[40] Zemlyanov D Y *et al* 2018 Versatile technique for assessing thickness of 2D layered materials by XPS *Nanotechnology* **29** 10

[41] Fadley C S 1978 *Electron Spectroscopy: Theory, Techniques and Applications* (New York: Academic) pp 1–156

[42] Scofield J H 1976 Hartree-slater subshell photoionization cross-sections at 1254 and 1487 eV *J. Electron Spectros. Relat. Phenomena* **8** 129–37

[43] Yeh J J and Lindau I 1985 Atomic subshell photoionization cross sections and asymmetry parameters: $1 \leqslant Z \leqslant 103$ *At. Data Nucl. Data Tables* **32** 1–155